Agricultural and Forest Meteorology 324 (2022) 109115

Contents lists available at ScienceDirect

Agricultural and Forest Meteorology

journal homepage: www.elsevier.com/locate/agrformet

Causality guided machine learning model on wetland CH_4 emissions across global wetlands

Kunxiaojia Yuan [a], Qing Zhu [a,*], Fa Li [a,c], William J. Riley [a], Margaret Torn [a], Housen Chu [a], Gavin McNicol [b], Min Chen [c], Sara Knox [d], Kyle Delwiche [e], Huayi Wu [f], Dennis Baldocchi [e], Hongxu Ma [g], Ankur R. Desai [h], Jiquan Chen [i], Torsten Sachs [j], Masahito Ueyama [k], Oliver Sonnentag [l], Manuel Helbig [m], Eeva-Stiina Tuittila [n], Gerald Jurasinski [o], Franziska Koebsch [p], David Campbell [q], Hans Peter Schmid [r], Annalea Lohila [s], Mathias Goeckede [t], Mats B. Nilsson [u], Thomas Friborg [v], Joachim Jansen [w], Donatella Zona [x], Eugenie Euskirchen [y], Eric J. Ward [z], Gil Bohrer [aa], Zhenong Jin [ab], Licheng Liu [ab], Hiroki Iwata [ac], Jordan Goodrich [q], Robert Jackson [ad]

[a] Climate and Ecosystem Sciences Division, Climate Sciences Department, Lawrence Berkeley National Laboratory, Berkeley, CA, USA
[b] Department of Earth and Environmental Sciences, University of Illinois at Chicago, Chicago, IL, USA
[c] Department of Forest and Wildlife Ecology, University of Wisconsin-Madison, Madison, WI, USA
[d] Department of Geography, The University of British Columbia, Vancouver, British Columbia, Canada
[e] Department of Environmental Science, Policy, and Management, University of California, Berkeley, CA, USA
[f] State Key Laboratory of Information Engineering in Surveying, Mapping and Remote Sensing, Wuhan University, Wuhan, China
[g] Department of Geography, University of California, Berkeley, CA, USA
[h] Department of Atmospheric and Oceanic Sciences, University of Wisconsin-Madison, Madison, WI, USA
[i] Department of Geography, Environment, and Spatial Sciences, Michigan State University, East Lansing, MI, USA
[j] GFZ German Research Centre for Geosciences, Potsdam, Germany
[k] Graduate School of Life and Environmental Sciences, Osaka Prefecture University, Sakai, Japan
[l] Département de Géographie, Université de Montréal, Montréal, QC, Canada
[m] Department of Physics and Atmospheric Science, Dalhousie University, Halifax, NS, Canada
[n] School of Forest Sciences, University of Eastern Finland, Joesnuu, Finland
[o] Landscape Ecology, University of Rostock, Rostock, Germany
[p] Digital Forest, University of Göttingen, Göttingen, Germany
[q] School of Science, University of Waikato, Hamilton, New Zealand
[r] Karlsruhe Institute of Technology, Institute of Meteorology and Climate Research, Karlsruhe, Germany
[s] Institute for Atmospheric and Earth System Research/Forest Sciences, University of Helsinki, Helsinki, Finland
[t] Department of Biogeochemical Signals, Max Planck Institute for Biogeochemistry, Jena, Germany
[u] Department of Forest Ecology and Management, Swedish University of Agricultural Sciences, Umeå, Sweden
[v] Department of Geosciences and Natural Resource Management, University of Copenhagen, Copenhagen K, Denmark
[w] Department of Ecology and Genetics, Uppsala University, Uppsala, Sweden
[x] Department of Biology, San Diego State University, San Diego, CA, USA
[y] Institute of Arctic Biology, University of Alaska Fairbanks, Fairbanks, AK, USA
[z] U.S. Geological Survey, Wetland and Aquatic Research Center, Lafayette, LA, USA
[aa] Department of Civil, Environmental & Geodetic Engineering, Ohio State University, Columbus, OH, USA
[ab] Department of Bioproducts and Biosystems Engineering, University of Minnesota, St Paul, MN, USA
[ac] Department of Environmental Science, Faculty of Science, Shinshu University, Matsumoto, Japan
[ad] Department of Earth System Science, Stanford University, Stanford, CA, USA

A R T I C L E   I N F O

Keywords:
Eddy covariance CH_4 emission
Wetlands

A B S T R A C T

Wetland CH_4 emissions are among the most uncertain components of the global CH_4 budget. The complex nature of wetland CH_4 processes makes it challenging to identify causal relationships for improving our understanding and predictability of CH_4 emissions. In this study, we used the flux measurements of CH_4 from eddy covariance

* Corresponding author.
E-mail address: qzhu@lbl.gov (Q. Zhu).

https://doi.org/10.1016/j.agrformet.2022.109115
Received 11 February 2022; Received in revised form 22 July 2022; Accepted 4 August 2022
Available online 11 August 2022

Causal inference
Machine learning

towers (30 sites from 4 wetlands types: bog, fen, marsh, and wet tundra) to construct a causality-constrained machine learning (ML) framework to explain the regulative factors and to capture CH_4 emissions at sub-seasonal scale. We found that soil temperature is the dominant factor for CH_4 emissions in all studied wetland types. Ecosystem respiration (CO_2) and gross primary productivity exert controls at bog, fen, and marsh sites with lagged responses of days to weeks. Integrating these asynchronous environmental and biological causal relationships in predictive models significantly improved model performance. More importantly, modeled CH_4 emissions differed by up to a factor of 4 under a $+1^{\circ}C$ warming scenario when causality constraints were considered. These results highlight the significant role of causality in modeling wetland CH_4 emissions especially under future warming conditions, while traditional data-driven ML models may reproduce observations for the wrong reasons. Our proposed causality-guided model could benefit predictive modeling, large-scale upscaling, data gap-filling, and surrogate modeling of wetland CH_4 emissions within earth system land models.

1. Introduction

Methane (CH_4) has been the second most important contributor to post-industrial global warming after carbon dioxide (CO_2), with a Global Warming Potential (GWP) of 28-34 times of CO_2 over a 100-year time horizon (Bergamaschi et al., 2013; IPCC, 2013). Wetland CH_4 emissions are the largest natural global sources, contributing around 20-30% to global emissions (Bousquet et al., 2006; Chen and Prinn, 2006; Saunois et al., 2020). Global warming (Koffi et al., 2020), anthropogenic emissions (Boothroyd et al., 2017), wetland expansion (Zhang et al., 2017), and increasing methanogenic substrate availability (Schuur et al., 2008) are expected to increase CH_4 emissions and thereby amplify climate warming (Tao et al., 2020). Freshwater wetlands remain the largest and most uncertain natural CH_4 source to the atmosphere (Peltola et al., 2019; Saunois et al., 2020), but with considerable discrepancies among bottom-up biogeochemistry models, top-down atmospheric inversion models, and data-driven machine learning models (Koffi et al., 2020; Peltola et al., 2019; Saunois et al., 2020). Therefore, improvements in the understanding of uncertainty sources and development of robust modeling frameworks for CH_4 emissions are required to estimate present-day and future wetland CH_4 emissions (Dean et al., 2018).

Wetland CH_4 emissions are affected by multiple environmental (*e.g.*, temperature, redox conditions) and biological (*e.g.*, plant photosynthesis, microbial enzyme activity) factors (Delwiche et al., 2021; Knox et al., 2021). Wetland CH_4 is produced by methanogens under anaerobic conditions (Mayer and Conrad, 1990), with the production rate controlled by multiple drivers such as temperature, availability of substrate (Bergman et al., 2000; Schaufler et al., 2010; Whalen, 2005), O_2, and alternative electron acceptors (Pasut et al., 2021). After production, CH_4 can be emitted to the atmosphere through various pathways (*e.g.*, diffusion, ebullition, plant aerenchyma transport) that are affected by temperature, water depth, air pressure, and plant aerenchyma properties (Bastviken, 2009; Knox et al., 2021; Morin et al., 2014; Rey-Sanchez et al., 2018; Villa et al., 2020). CH_4 can be oxidized by aerobic bacteria when passing through oxic soil or water during transport (Wahlen, 1993) or even via anaerobic pathways (anaerobic oxidation of methane, AOM) (Fan et al., 2021). The impacts of environmental and biological factors on CH_4 emissions are often non-linear and operate over a range of time scales (Sturtevant et al., 2016). For example, the response of CH_4 production to temperature is observed to be hysteretic (Chang et al., 2021) due to seasonal substrate availability and microbial activity (Chang et al., 2020). The response of CH_4 emissions to GPP may be delayed and the relationship between them has been observed to be lagged by hours to days (Hatala et al., 2012a; Rinne et al., 2018), while CH_4 emission responses to water table fluctuations can be lagged by days to months (Chen et al., 2021; Goodrich et al., 2015; Sturtevant et al., 2016). The multi-driver dependency, nonlinearity, and time-lagged characteristics make it challenging to understand how CH_4 emissions interact with environmental and biological factors and to accurately represent them in predictive models (Kim et al., 2020; Sturtevant et al., 2016; Turner et al., 2021).

In most ecosystem biogeochemical models, wetland CH_4 production is represented as a function of net primary production and/or heterotrophic respiration (as a proxy for microbial activity), with both constrained by environmental scalars (Melton et al., 2013; Wania et al., 2013; Xu et al., 2016). For example, temperature sensitivity scalars have been proposed based on observed CH_4 emissions (Yvon-Durocher et al., 2014). However, *in situ* observations reveal high variability and uncertainty in CH_4 emissions even with nearly identical environmental conditions (Chadburn et al., 2020; Granberg et al., 1997; Hemes et al., 2018; Koch et al., 2014; Rinne et al., 2018; Villa et al., 2021; Zona et al., 2016), implying much more complex functional relationships between CH_4 emissions and environmental and biological factors. A few ecosystem models explicitly represent more of the underlying microbial, plant, and abiotic processes leading to wetland CH_4 emissions (*e.g., ecosys* (Grant et al., 2015; Grant et al., 2017a; Grant et al., 2017b), BAMS4 (Pasut et al., 2021), and JSBACH-methane (Castro-Morales et al., 2018)) and confirm that these nonlinear interactions should be considered to improve model predictions of methane emissions (Chang et al., 2019).

In addition to the ecosystem biogeochemical models, Machine Learning (ML) models are becoming useful tools for capturing complex nonlinear relationships, and have achieved good performance in gap filling CH_4 emission data (Hatala et al., 2012a; Hatala et al., 2012b; Irvin et al., 2021; Kim et al., 2020; Knox et al., 2019; Morin et al., 2014) and spatial upscaling (Peltola et al., 2019). However, widely-applied ML frameworks do not accurately represent lagged CH_4 emission dependencies (Kim et al., 2020). Including lagged variables as predictors may improve ML model performance, but risks overfitting, especially for multiple-driver dominated ecosystems with limited temporal observations (Kim et al., 2020). Furthermore, commonly used ML models do not consider causality constraints (Pearl, 2019; Reichstein et al., 2019). Such ML models may fit an observational dataset well while not being driven by causal relationships (Pearl, 2019; Runge et al., 2019a). In this study, we explore whether an ML model that represents lagged responses and considers underlying causal relationships can improve process understanding and wetland CH_4 emission predictions.

We used CH_4 emission measurements at 30 eddy covariance towers covering 4 wetland types (bog, fen, marsh, and wet tundra), to test three hypotheses: (1) It is possible to infer with statistical confidence causal relationships between drivers and CH_4 emissions. (2) The environmental drivers significantly affecting methane emissions differ among the wetlands by their type and location. (3) Future model predictions that are well calibrated based on current flux observations, but differ in their assumed causal relationships between drivers and methane emissions, will diverge significantly. To test these hypotheses, we develop an integrated framework that combines causality and ML to improve understanding of causal relationships affecting CH_4 emissions and modeling of wetland CH_4 emissions across various wetland ecosystems. In this work, a causal relationship exists between predictor (X) and CH_4 emissions if, when excluding the confounding effects from other predictors and from the history of CH_4 emissions, knowing the predictor (X) could significantly reduce the uncertainty in predicting CH_4 emissions (Abdul Razak and Jensen, 2014; Runge et al., 2019a). The overarching goal of this study is to develop, train, and validate a ML model to improve predictive modeling of wetland CH_4 emission for diverse wetlands.

2. Methodology

2.1. Study sites and data description

The dataset used in this study is from the FLUXNET-CH_4 synthesis activity, which compiles, standardizes, and gap-fills available daily eddy covariance CH_4 emission data, via the regional networks of AmeriFlux, EuroFlux, OzFlux, and AsiaFlux (Delwiche et al., 2021; Knox et al., 2019). We focus on four types of natural freshwater wetlands (bog, fen, marsh, and wet tundra), and use 30 wetland sites, each with at least one year of CH_4 observations (Fig. 1; Table 1). The wetland classification is based on the site-specific literature (Delwiche et al., 2021). Daily CH_4 emissions (F_{CH_4}) and 13 potential drivers are considered in our analysis: Air Temperature (T_a), Topsoil Temperature (T_s) (detailed information of soil temperature depth can be seen in Delwiche et al. (2021)), Water Table Depth (D_{wt}), Precipitation (P), Soil Water Content (θ), Relative Humidity (RH), Vapor Pressure Deficit (VPD), Atmospheric Pressure (PA), Wind Speed (WS), and Incoming Shortwave Radiation (SW); and biological factors: Gross Primary Production (GPP), Ecosystem Respiration (RECO), and Net Ecosystem Exchange (NEE) (See variable availability for each site in Table S1). These variables are widely acknowledged as important driving factors for wetland CH_4 emissions (Knox et al., 2021; Oertel et al., 2016). Details of data standardization for the FLUXNET-CH_4 dataset are presented in Knox et al. (2019). In this study, we used the observed non-gap-filled measurements to maintain the original dynamic patterns and avoid potential biases from the gap-filling algorithms that have their own assumed causal relationships.

2.2. Transfer entropy analysis

We employ a transfer entropy approach with PCMCI framework (Runge et al., 2019b) to identify non-linear directional relationships between environmental and biological factors and F_{CH_4}. Transfer entropy is a powerful tool to reveal the causality for non-linear and asynchronous systems (Bouskill et al., 2020; Liu et al., 2019; Schreiber, 2000). The approach quantifies information entropy flow from source variables (*e.g.*, T_a) to the target variable (F_{CH_4}) by measuring the information entropy reduction in the target variables when excluding effects from various confounders (Yuan et al., 2022; Li et al., 2022). If transfer entropy is statistically significant, the causal relationship from a source variable to the target variable is confirmed. For each pair of variables of interest, we calculate the transfer entropy (T) from source variable X to a target variable Y considering the confounders of Z (Schreiber, 2000):

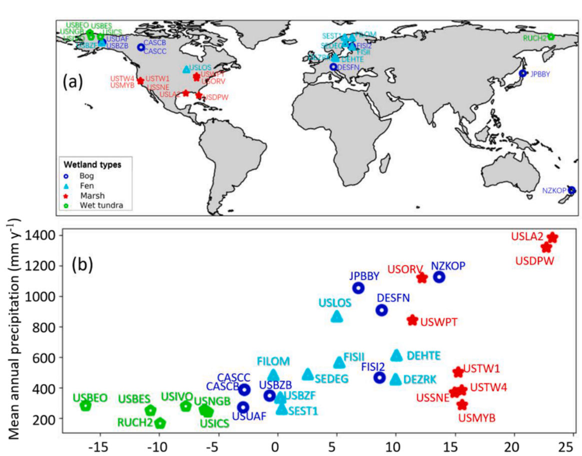

Fig. 1. (a) Geographic locations and wetland types of the 30 selected eddy covariance sites. (b) Mean annual temperature and precipitation of each site.

$$T(X \to Y) = \sum_{y_t, z, x_t^{[l]}} p\left(y_t, z, x_t^{[l]}\right) \log_2 \frac{p\left(y_t \middle| \left(z, x_t^{[l]}\right)\right)}{p(y_t|z)} \tag{1}$$

where l is the corresponding time lag of source variable X. p is the probability density. Compared with the linear and nonlinear correlation based methods (*e.g.*, mutual information in Knox et al. (2021)), transfer entropy can explicitly exclude confounding effects when detecting the causal strength from one variable to F_{CH_4} through removing shared information between confounders (Z) and the target variable (Y).

In theory, all potential confounders should be included when identifying causal relationships. However, in practice, too many confounders will cause high dimensionality and statistical instability issues (Runge et al., 2019a; Yuan et al., 2021). For simplicity, previous studies often considered the immediate history of a target variable as the confounder, assuming that it contributes the most confounding information to the target (Ruddell and Kumar, 2009; Yuan et al., 2021). However, wetland F_{CH_4} can be jointly regulated by multiple factors including the history of F_{CH_4}. To minimize the interferences from important confounders and to avoid high dimensionality, we adaptively considered three confounders that have the strongest control on the variation of F_{CH_4} through the PCMCI framework (Runge et al., 2019b). PCMCI contains two key steps: (1) PC (named after its inventors Peter and Clark) (Spirtes et al., 2000) and (2) Momentary Conditional Independency (MCI) (Runge et al., 2019b). To infer the causal strength from a source variable to the target variable, we firstly used the transfer entropy method in PC to rank the contribution of all potential confounders (*e.g.*, air temperature, soil water content) with relative lower dimensionality (Spirtes et al., 2000), and used transfer entropy in MCI to calculate the causal strength from a source variable to the target variable by excluding the information entropy from the most important confounders (Runge et al., 2019b). We iteratively conducted the causal inference process for each variable to obtain the causal strength (Fig. S1).

The shuffled surrogate method (Kantz and Schürmann, 1996) was employed to test the statistical significance of transfer entropy. This method randomly shuffles source and target time series to destroy time correlations. Shuffled surrogate transfer entropy was computed 100 times through Monte Carlo simulations. A one-tailed significance test is then applied to determine the 95% confidence of the transfer entropy (Ruddell and Kumar, 2009).

2.3. CH_4 emission predictive models

We develop a causality constrained interpretable ML model based on the Long-Short-Term-Memory framework (Guo et al., 2019a; Hochreiter and Schmidhuber, 1997; Li et al., 2020) for prediction (hereafter causal-LSTM). We compared the causal-LSTM model performance, internal functional relationships, and model sensitivity against its baseline LSTM model (described below), to illustrate the benefit of including causality constraints in prediction.

2.3.1. Baseline model

The baseline naïve LSTM model has been widely used in time sequence predictions (Alahi et al., 2016; Li et al., 2020). One of the advanced features of LSTM is the gate mechanism that controls the information flow to be memorized or forgotten, which enables capturing short-term and long-term dependencies underlying data sequences. Here, we use the LSTM model for prediction, given the lagged responses of emissions to environmental and biological factors. The recursive representations of LSTM and prediction can be represented as:

$$\begin{aligned} h_t,\ c_t &= f(x_t, h_{t-1},\ c_{t-1}) \\ \widehat{Y}_{T+1} &= W_l h_T + b_l \end{aligned} \tag{2}$$

where x_t (t is time step, $0<t \le T$) is the input vector, c_t is the cell memory state vector, and h_t represents the hidden state vector with useful

Table 1
FLUXNET-CH_4 site information of the 30 sites used in this analysis.

Wetland Type	Site ID	Site name	IGBP	LAT	LON	Startyear	Endyear	Data DOI	References
Bog	CA-SCB	Scotty Creek Bog	WET	61	-121	2014	2017	DOI: 10.18140/FLX/1669613	(Sonnentag and Helbig, 2020a)
	CA-SCC	Scotty Creek Landscape	ENF	61	-121	2013	2016	DOI: 10.18140/FLX/1669628	(Sonnentag and Helbig, 2020b)
	DE-SfN	Schechenfilz Nord	WET	48	11.33	2012	2014	DOI: 10.18140/FLX/1669635	(Schmid and Klatt, 2020)
	FI-Si2	Siikaneva II	WET	62	24.2	2012	2016	DOI: 10.18140/FLX/1669639	(Vesala et al., 2020a)
	JP-BBY	Bibai bog	WET	43	141.8	2015	2018	DOI: 10.18140/FLX/1669646	(Ueyama et al., 2020)
	NZ-Kop	Kopuatai	WET	-37	175.6	2012	2015	DOI: 10.18140/FLX/1669652	(Campbell and Goodrich, 2020)
	US-BZB	Bonanza Creek Thermokarst Bog	WET	65	-148	2014	2016	DOI: 10.18140/FLX/1669668	(Euskirchen and Edgar, 2020a)
	US-Uaf	University of Alaska, Fairbanks	ENF	65	-148	2011	2018	DOI: 10.18140/FLX/1669701	(Iwata et al., 2020)
Fen	DE-Hte	Huetelmoor/Rodewiese	WET	54	12.18	2011	2018	DOI: 10.18140/FLX/1669634	(Koebsch and Jurasinski, 2020)
	DE-Zrk	Zarnekow	WET	54	12.89	2013	2018	DOI: 10.18140/FLX/1669636	(Sachs and Wille, 2020)
	FI-Lom	Lompolojänkkä	WET	68	24.21	2006	2010	DOI: 10.18140/FLX/1669638	(Lohila et al., 2020)
	FI-Sii	Siikaneva I (FI-Sii)	WET	62	24.19	2013	2018	DOI: 10.18140/FLX/1669640	(Vesala et al., 2020b)
	SE-Deg	Degero	WET	64	19.56	2014	2018	DOI: 10.18140/FLX/1669659	(Nilsson and Peichl, 2020)
	SE-St1	Stordalen Mire	WET	65	19.05	2012	2014	DOI: 10.18140/FLX/1669660	(Jansen et al., 2020)
	US-BZF	Bonanza Creek Rich Fen	WET	65	-148	2014	2016	DOI: 10.18140/FLX/1669669	(Euskirchen and Edgar, 2020b)
	US-Los	Lost Creek	WET	46	-90	2014	2018	DOI: 10.18140/FLX/1669682	(Desai and Thom, 2020)
Marsh	US-DPW	Disney Wilderness Preserve Wetland	WET	28	-81.4	2013	2017	DOI: 10.18140/FLX/1669672	(Hinkle and Bracho, 2020)
	US-LA2	Salvador WMA Freshwater Marsh	WET	30	-90.3	2011	2013	DOI: 10.18140/FLX/1669681	(Holm et al., 2020)
	US-Myb	Mayberry Wetland	WET	30	-122	2011	2018	DOI: 10.18140/FLX/1669685	(Matthes et al., 2020)
	US-ORv	Olentangy River Wetland Research Park	WET	40	-83	2011	2015	DOI: 10.18140/FLX/1669689	(Bohrer and Morin, 2020)
	US-Sne	Sherman Island Restored Wetland	GRA	38	-122	2016	2018	DOI: 10.18140/FLX/1669693	(Shortt et al., 2020)
	US-Tw1	Twitchell Wetland West Pond	WET	38	-122	2011	2018	DOI: 10.18140/FLX/1669696	(Valach et al., 2020)
	US-Tw4	Twitchell East End Wetland	WET	38	-122	2013	2018	DOI: 10.18140/FLX/1669698	(Eichelmann et al., 2020)
	US-WPT	Winous Point North Marsh	WET	41	-83	2011	2013	DOI: 10.18140/FLX/1669702	(Chen and Chu, 2020)
Wet tundra	RU-Ch2	Chersky Reference	WET	69	161.4	2014	2016	DOI: 10.18140/FLX/1669654	(Göckede, 2020; Göckede et al., 2019)
	US-Beo	Barrow Environmental Observatory (BEO) tower	WET	71	-157	2013	2014	DOI: 10.18140/FLX/1669664	(Zona and Oechel, 2020a)
	US-Bes	Barrow-Bes (Biocomplexity Experiment South tower)	WET	71	-157	2013	2015	DOI: 10.18140/FLX/1669665	(Zona and Oechel, 2020b)
	US-ICs	Imnavait Creek Watershed Wet Sedge Tundra	WET	69	-149	2014	2016	DOI: 10.18140/FLX/1669678	(Euskirchen et al., 2020)
	US-Ivo	Ivotuk	WET	68	-156	2013	2016	DOI: 10.18140/FLX/1669679	(Zona and Oechel, 2020c)
	US-NGB	NGEE Arctic Barrow	SNO	71	-157	2012	2018	DOI: 10.18140/FLX/1669687	(Torn and Dengel, 2020)

information for predictions. In this study, x_t represents the biotic and abiotic drivers across sites; h_T is the hidden state vector at the last time step T; $\widehat{Y}_{T+1}$ is the predicted F_{CH_4} at the time step $T+1$; and W_l and b_l are the parameters that need to be learned. The f in Eq. (2) is an integrated function that includes five individual equations:

$$\begin{aligned} f_t &= \sigma\left(W_{xf}x_t + W_{hf}h_{t-1} + b_f\right) \\ i_t &= \sigma\left(W_{xi}x_t + W_{hi}h_{t-1} + b_i\right) \\ o_t &= \sigma\left(W_{xo}x_t + W_{ho}h_{t-1} + b_o\right) \\ c_t &= f_t \odot c_{t-1} + i_t \odot \tanh\left(W_{xc}x_t + W_{hc}h_{t-1} + b_c\right) \\ h_t &= o_t \odot \tanh(c_t) \end{aligned} \tag{3}$$

where f_t, i_t, and o_t are gating vectors that control how much information for the cell memory to forget, input/update, and output, respectively; σ is the sigmoid activation function; $\odot$ is element-wise product; W_{xf}, W_{hf}, W_{xi}, W_{hi}, W_{xo}, W_{ho}, W_{xc}, and W_{hc} are linear transformation matrices that need to be learned; and b_f, b_i, b_o, and b_c are corresponding bias vectors obtained through model training.

For the LSTM, we used the recursive feature elimination (RFE) method (Guyon et al., 2002) to remove spurious predictors. Specifically, we iteratively removed one predictor, used the remained predictors to train the LSTM, and calculated the correlation coefficient between observations and predictions after removing the predictor. Then, we removed the weakest predictor which showed the lowest impacts on model performance, and repeated the predictor elimination process until only one predictor was left. Finally, we present LSTM modeling results based on the subset of predictors selected by RFE method that have the highest model performance.

2.3.2. Causality constrained LSTM

Although baseline LSTM is capable of capturing short-term and long-term dependencies in the input time series, it works as a black-box and cannot explicitly select important driving variables and lacks interpretability of its predictions. Also, the dependencies identified within the LSTM model are based on correlations rather than causality (a more informative directional relationship). To this end, the LSTM model can be improved through attention mechanism, an effective weight assignment method, to increase its transparency (Alahi et al., 2016; Guo et al., 2019a; Li et al., 2020; Liang et al., 2018; Qin et al., 2017; Vaswani et al., 2017). The weight mechanism explicitly and dynamically assigns larger weights to more important variables, thereby improving model performance and interpretability (Guo et al., 2019a; Li et al., 2020). However, without the guide or constraint of causality, the correlation-based ML models may represent wrong processes (*e.g.*, mis-capture dominant causal drivers) (Moraffah et al., 2020; Pearl, 2019; Runge et al., 2019b), making the model unreliable, especially for predictions using multiple drivers with similar seasonal trends (confounding) information under climate change (Runge et al., 2019a). In addition, we further imposed additional constraints using causal relationships from input variables to the target variable and led to the causal-LSTM model. The causal-LSTM model first calculated the causal relationship using transfer entropy. And then through optimization, it reduced the model biases on both prediction error and structure difference between model captured variable dependency and observation-based causal strength. Below, we introduce the weight assignment mechanism (attention mechanism) in the LSTM approach and describe details of how we incorporate causality constraints in the model.

Similar to the baseline LSTM, the ith driving variable at time step t can be iteratively transformed to a hidden state vector h_t^i through the gate mechanism Guo et al., 2019a; Hochreiter and Schmidhuber, 1997; Li et al., 2020; Qin et al., 2017). To represent the importance of the ith variable at time step t, a weight, w_t^i *or* $w_t^{i'}$ is dynamically calculated through Eqs. (4) and ((5), and assigned to h_t^i. Then, the weighted summation h_{sum}^i of h_t^i across time steps is obtained to represent the summarized information for the ith driving variable:

$$w_t^i = \tanh\left(W_p h_t^i\right) \tag{4}$$

$$\mathrm{w}_t^{i'} = \frac{e^{\mathrm{w}_t^i}}{\sum_{t_0=1}^{T} e^{\mathrm{w}_{t_0}^i}} \tag{5}$$

$$h_{sum}^i = \sum_{t=1}^{T} w_t^{i'} h_t^i \tag{6}$$

Where W_p is a parameter matrix that needs to be learned, and tanh is the hyperbolic tangent function. T is the total number of time steps.

To further represent the relative importance of the ith driving variable compared to other driving variables, a weight, α_i, is obtained and normalized as α_i':

$$\alpha_i = \tanh\left(W_a\left[h_{sum}^i, h_T^i\right]\right) \tag{7}$$

$$\alpha_i' = \frac{e^{\alpha_i}}{\sum_{j=1}^{n} e^{\alpha_j}} \tag{8}$$

where W_a is a learnable parameter matrix.

Finally, using the weighted sum of all driving variables, the model generates the prediction $\widehat{Y}_{T+1}$:

$$o_i = W_o\left[h_{sum}^i, h_T^i\right] + b_o \tag{9}$$

$$\widehat{Y}_{T+1} = \sum_{i=1}^{n} o_i \alpha_i' \tag{10}$$

where the linear function with weight W_o and bias b_o, along with weight α_i' produce the final prediction.

To make the internal structure of the model more consistent with underlying physical processes, we use transfer entropy inferred causal relationships to constrain the variable importance (variable weight) in the predictive model. A larger transfer entropy from a driver (*e.g.*, soil temperature) to F_{CH_4} implies variations of the driver can cause larger variations in CH_4 emissions, compared to other drivers (Ruddell and Kumar, 2009). Similarly, a larger variable weight (α_i') indicates that the i^{th} variable plays more important roles in modeling the target variable (Guo et al., 2019a; Li et al., 2020; Liang et al., 2018; Qin et al., 2017). To guide the model to learn dependencies between causally dominant drivers and F_{CH_4}, we measure the difference between transfer entropy inferred feature importance vector α_{TE} and that of the model captured feature importance vector α_k for each sample k, and integrate the difference along with modeled errors into the final loss function (Eq. (11)). In the vector α_{TE}, α_{TE_i} represents the transfer entropy from the ith driving variable to F_{CH_4}. In α_k, $\alpha_{k,i}$ represents the ith variable weight, α_i', for a sample k. Each vector is divided by its summation to obtain a probability distribution ranging from 0 to 1, and KL-Divergence (Kullback and Leibler, 1951) (the second item in the loss function, Eq. (11)) is used to measure the distribution difference between the two vectors:

$$Loss = \frac{1}{N}\sum_{k=1}^{N}\left(\widehat{Y}_k - Y_k\right)^2 + \lambda\sum_{k=1}^{N}\sum_{i=1}^{n}\alpha_{TE_i}\left|\log\frac{\alpha_{TE_i}}{\alpha_{k,i}}\right. \tag{11}$$

where λ is a structural punishment parameter, and a larger λ means that the model puts more emphasis on structural similarity instead of errors. In Eq. (11), the first right hand side term is the errors between observations and predictions, while the second term is the structural similarity between causality inferred feature importance and importance the model captured. N is the number of predicted data samples, and n is the number of variables. The baseline LSTM uses only the first term on the right-hand side for the loss function, while the causal-LSTM has additional constraint from causal relationships via the second term (Eq. (11)).

The model parameters are learned via a back-propagation algorithm (Rumelhart et al., 1986) by minimizing the integrated loss (Eq. (11)) with a variational dropout to avoid overfitting (Gal and Ghahramani, 2016). We used the intra-site validation scheme to test model performance on capturing intra-site temporal variations of F_{CH_4}. Specifically, in each experiment, for each site, we randomly sampled 80% of data as a training dataset, remained 10% as a validation dataset (used to avoid overfitting during training (Prechelt, 1998)), and retained the remaining 10% as a test dataset (a holdout dataset used to unbiasedly evaluate the final model). We repeated each experiment 20 times to reduce model bias due to random data selection. We compared the model performance with different λ values (Fig. S2), and selected the best one (λ=0.005) that has the lowest prediction errors. To evaluate the lag effects for model improvement, we varied the lengths (one-week vs. one-month) of time series input used in the models. In addition, we also used the leave-one-site-out scheme (here referred as inter-site validation) (Jung et al., 2011) to test model performance on spatial extrapolation of F_{CH_4} on each tested site. Other detailed experimental settings of each model are listed in Table S2.

3. Results

3.1. Causal relationships derived from transfer entropy

Transfer entropy analysis revealed that daily F_{CH_4} was most strongly driven by soil temperature (T_s) in the four analyzed wetland ecosystem types (bog, fen, marsh, and wet tundra; Fig. 2a), with a range of different time lags. The statistics of dominant drivers at each individual site also showed that T_s dominated in most sites (Fig. S3). Furthermore, the strength of the $T_s \rightarrow F_{CH_4}$ relationship declined with increasing mean air temperature (slope = -0.0014, R value = -0.63, p value <0.05) (Fig. 2b). This inverse relationship suggested that CH_4 emissions in colder regions were more sensitive to temperature than in warmer areas. The control from air temperature (T_a) was weaker than that from T_s and was prominent only at fen and marsh wetlands (Fig. 2a).

Two biological factors, Ecosystem Respiration (RECO) and plant Gross Primary Production (GPP), also exerted strong controls on daily F_{CH_4} in bog, fen, and marsh wetlands. These strong relationships between F_{CH_4} and vegetation carbon turnover are consistent with the findings of many previous studies (Hatala et al., 2012a; Mitra et al., 2020; Rinne et al., 2018). Plant GPP stimulates CH_4 production indirectly by providing carbon input, mainly via root exudates fueling microbial activity, which produces substrates (such as acetate and CO_2) for acetotrophic and hydrogenotrophic methanogenesis (Bastviken, 2009; Mitra et al., 2020; Ström et al., 2012; Whiting and Chanton, 1993). Additionally, GPP can be seen as a proxy of plant-mediated CH_4 transport via aerenchyma tissue (Bastviken, 2009; King et al., 1998; Turetsky et al., 2014). Previous studies argued that the relationship between GPP and F_{CH_4} may be due to covariation with confounding drivers (*e.g.*, soil temperature) (Chang et al., 2021; Knox et al., 2019). In this study, we confirmed the existence of a strong coupling from GPP and RECO with F_{CH_4} by removing confounding effects when identifying the causal relationships across multiple wetland types.

Compared with temperature and biological factors, the controls from other variables on F_{CH_4} were much weaker (Figs. 2a, S3) and less consistent across wetland types. For example, VPD controlled F_{CH_4} more at bog and fen ecosystems, while *PA* showed weak causal relationships with F_{CH_4} across all sites. For water-related factors, significant controls on F_{CH_4} existed only at a few sites, which may be attributed to limited observations of water table depth (D_{wt}, 16 sites) and soil water content (θ, 9 sites), and limited variations of soil wetness across studied sites (more details are discussed in Section 4.1).

3.2. F_{CH_4} predictions with causal constraints

Because causal relationships varied across wetland ecosystems, we trained independent ML models for each wetland type (bog, fen, marsh, and wet tundra). Two types models were considered: Long Short-Term Memory (LSTM) and causality-constrained interpretable LSTM (causal-LSTM). We found that Causal-LSTM performed consistently better than LSTM for all four wetland types with higher Pearson correlation coefficient (R) and lower relative MAE (mean absolute error) when inputting four weeks of historical drivers (Table S3 and S4). For example, *R* values in LSTM ranged from 0.861 to 0.908 and relative MAE ranged from 0.271 to 0.433, while R in causal-LSTM ranged from 0.904 to 0.921 and relative MAE ranged from 0.217 to 0.368 (Fig. 3, Tables S3 and S4). Consistently, with one week of inputs, the causal-LSTM also showed significantly higher R and lower relative MAE compared with LSTM in all wetland types ($p < 0.05$, Tables S5 and S6). We also compared the causal-LSTM approach with four other widely used ML algorithms (random forest, decision tree, artificial neural networks, and support vector machine), and found that causal-LSTM had the highest prediction accuracy (Fig. S4), with R value of 0.94 between observations and predictions of causal-LSTM across all sites (Fig. S5).

For model evaluation with the inter-site validation scheme, causal-LSTM also performed reasonably well with R value of 0.75 between observations and predictions (Fig. S6) and lower biases than that of LSTM (Table S7). However, the inter-site validation performance of causal-LSTM dropped, compared with the intra-site validation scheme

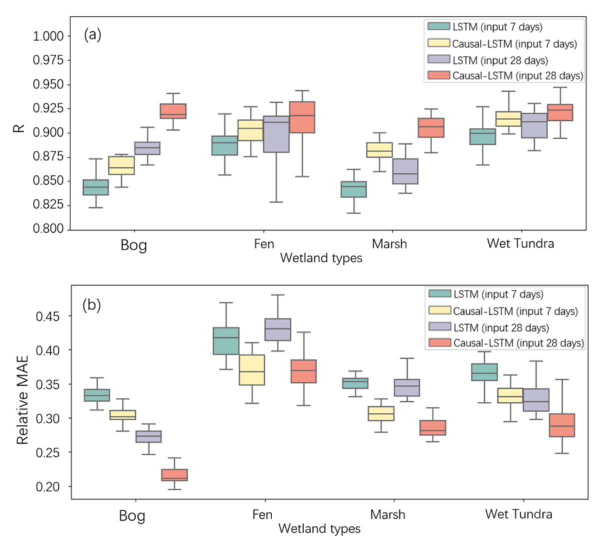

Fig. 3. Model performance comparison with different input lengths for LSTM (green and purple boxes) and causal-LSTM (yellow and red boxes), in terms of (a) correlation coefficient (R), and (b) relative MAE between predictions and observations. The boxes represent 25th to 75th percentiles, and the whiskers represent 5th to 95th percentiles of R or MAE for each wetland type.

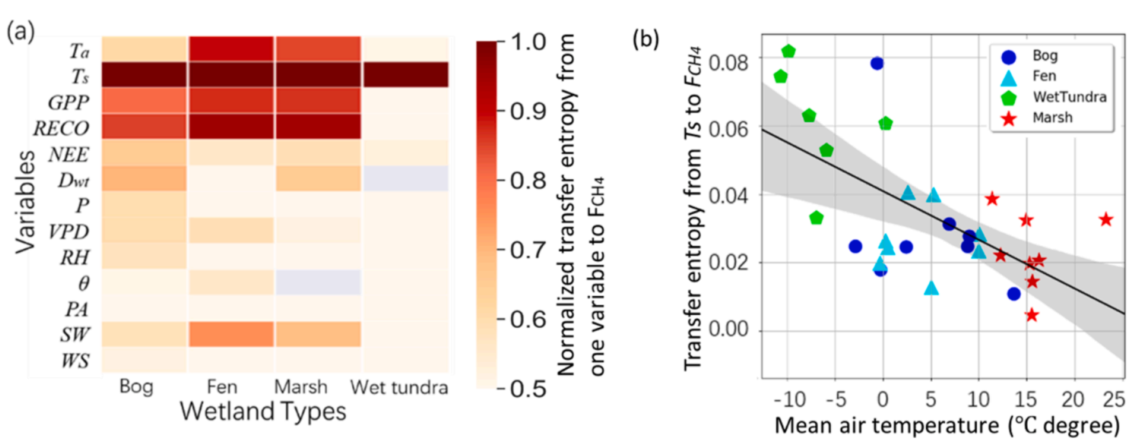

Fig. 2. (a) Causal relationships between environmental and biological factors and daily F_{CH_4} averaged across sites within four wetland ecosystems. Colors in the grid squares show the strength of transfer entropy (normalized to range from 0 to 1) from each variable to F_{CH_4}; darker colors represent larger values (a grey grid means that the observation data is unavailable). (b) Relationship between the strength of $T_s \rightarrow F_{CH_4}$ relationships and site Mean Annual Temperature (MAT); the grey bounds show a 95% confidence interval.

especially for the marsh (the mean R value dropped to 0.81 in bog, 0.81 in fen, 0.86 in wet tundra, and 0.69 in marsh), which may be due to the strong spatial heterogeneity of F_{CH_4} magnitude (e.g., mean CH_4 emission ranged from 2.706 nmol m^{-2} s^{-1} to 165.472 nmol m^{-2} s^{-1} across different sites) and environmental conditions (e.g., annual precipitation in marsh varied from ~200 to ~1400 mm/year). Overall, we conclude that the causal-LSTM provides the most effective approach to model wetland F_{CH_4}.

The results showed that model performance tended to be improved as the length of input time series increased from one to four weeks for both causal-LSTM (Fig. 3a and b, yellow vs. red bars) and LSTM models (Fig. 3a and b, green vs. purple bars). For R, the performance of both models at bog, and marsh was significantly ($p < 0.05$; Tables S8 and S9) improved as the input data length increased. Similarly, in terms of relative MAE, the causal-LSTM model showed significantly lower biases ($p < 0.05$; Table S10) in bog, marsh, and wet tundra ecosystems, and LSTM showed significant lower biases in bog and wet tundra ($p<0.05$, Table S11). Overall, longer histories of drivers (*i.e.*, memories) can provide additional information for predictions, especially in bog, marsh, and wet tundra.

4. Discussions

4.1. Soil temperature versus soil water control on F_{CH_4}

Wetland CH_4 emissions are regulated by multiple biotic (*i.e.*, production, oxidation) and abiotic (*i.e.*, advection, diffusion) processes, with each posting different dependencies on environmental factors. Therefore, the emergent relationships between wetland methane emissions and the corresponding environmental factors are expected to be complex and diverse across different wetland ecosystem types and across sites with different climate conditions (Turetsky et al., 2014). Among those environmental variables, previous studies have identified temperature and soil water content as major abiotic drivers for wetland CH_4 emissions (Knox et al., 2021; Song et al., 2011; Strachan et al., 2015) because soil water saturation and warm soil conditions are two prerequisites for anaerobic production of wetland CH_4 (Riley et al., 2011).

Here, we found strong soil temperature control on CH_4 emissions across bog, fen, marsh, and wet tundra ecosystems. The stronger causal relationship of $T_s \rightarrow F_{CH_4}$ compared to $T_a \rightarrow F_{CH_4}$ is consistent with the hypothesis that air temperature may decouple from soil temperature in colder ecosystems (*e.g.*, wet tundra) due to snow insulation of the ground (Kim et al., 2007). Similar strong correlations between T_s and wetland F_{CH_4} have been reported in numerous site-level studies (Granberg et al., 1997; Knox et al., 2021; Morin, 2019).

We also found relatively weak control from soil water related variables (Fig. 2), admit low confidence because of limited data. For example, soil water content had weak control in fen ecosystems, and water table depth had moderate control in bog and marsh ecosystems, but not in fen or wet tundra ecosystems. The lack of sensitivity may partly be due to the data quality of water related variables (D_{wt} is available in ~50% of our studied 30 sites, and θ is available in only ~30% of the 30 sites (Table S1)). Another potential reason is the fact that the sites used in this study all experienced relatively low variation of D_{wt} (mean standard deviation is 10.6 cm). Strong seasonal fluctuations of soil water are more expected at rice paddy or tropical swamp ecosystems (Jauhiainen et al., 2005; Mezbahuddin et al., 2014), which are not included in this study. For example, water table depth could vary ~80 cm at a managed rice paddy site in northern California and plays an important role in driving CH_4 emissions during both growing season and fallow periods (Knox et al., 2016). Although not frequently occurred, extreme droughts may result in significantly different water table at fen and bog sites that will reduce the methane emission (Brown et al., 2014; Rinne et al., 2020). However, ML model was trained with majority of the data to capture non-extreme conditions. In addition, we note that several studies reported weak dependencies between D_{wt} and F_{CH_4} (Jackowicz-Korczyński et al., 2010; Rinne et al., 2007; Rinne et al., 2018). Given the limitations in sites and water-related data availability, our results highlight the need for more eddy covariance and ancillary measurements in bog, fen, marsh, and wet tundra ecosystems, particularly measurements under long-term drying and rewetting conditions, or experiencing natural flooding and water table fluctuation. These observations will facilitate a more complete picture of how various factors affect wetland CH_4 emissions within these wetland ecosystems.

4.2. Causal relationships inform model evaluation and development

In addition to commonly used model evaluation metrics (*e.g.*, MAE and R), causal inference provided additional metrics to evaluate and benchmark models in terms of internal causal structures. Causal relationships may also help select process-based models with model causal structures similar to those in observations. In this analysis, we found that methane ML models can achieve comparable performance even though they have diverse causal relationships. We visualized variable importance within LSTM and causal-LSTM models and validated the modeled relationships against observed causal relationships identified by transfer entropy analysis (Fig. 4). The feature importance of causal-LSTM and LSTM were calculated according to attention weight statistics (Guo et al., 2019b; Li et al., 2020) and the feature importance derived from RFE (Guyon et al., 2002; Meyer et al., 2019) of 20 repeated experimental results, respectively, and were both normalized to 0~1. We found that LSTM mainly used dependencies from wind, atmospheric pressure, soil and air temperature, and total ecosystem respiration to estimate F_{CH_4}, which were different from those inferred from observations and causal-LSTM (Fig. 4). The feature importance in the causal-LSTM model is much more consistent with observations, confirming the effectiveness of the causality constraints.

The inferred causal relationships from biological and environmental variables on CH_4 emissions vary across different wetland types and time windows. Our results show that soil temperature dominantly controls F_{CH_4} in wet tundra, while biotic variables along with soil temperature co-dominate F_{CH_4} in fens, bogs, and marshes. The different controls imply that different ecosystems need to be considered separately in machine learning model development (Turetsky et al., 2014). Also for each wetland ecosystem, the responses of F_{CH_4} rely on processes with short time lags (*e.g.*, CH_4 transport, microbial activity) and long time lags (*e.g.*, fine-root turnover). Integrating both short and long causal relationships may also improve model performance.

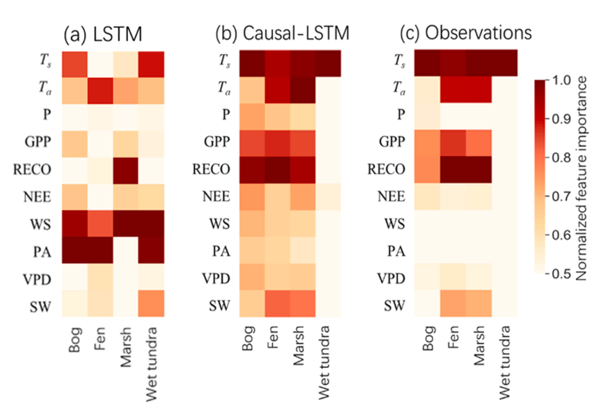

Fig. 4. Comparison of feature importance in (a) LSTM, (b) causal-LSTM, and (c) observations. Colors show the corresponding normalized feature importance that is normalized between 0 and 1, with higher value indicating higher importance.

4.3. Implications of considering causal relationships in CH_4 emission projections

Our results, in line with previous studies, suggest that data-driven ML models may accurately reproduce observations with the wrong reasons (Pearl, 2019; Reichstein et al., 2019; Runge et al., 2019a). The different causal relationships built within predictive models are critically important for climate change projections, since the responses of CH_4 emissions to climate change strongly depend on the strength of the underlying causal relationships. Thus we hypothesized that although both LSTM and causal-LSTM performed reasonably well under present-day conditions, their predictions under warming climate could differ due to their differences in internal functional relationships, or altered combinations of forcing mechanisms. To test this hypothesis, we conducted a theoretical soil warming experiment (+1 °C) at all sites through modeling. We acknowledged that more complex changes can occur in a real soil warming experiment (*e.g.*, soil drying caused by warming) (Pries et al., 2017). However, this simple soil warming experiment isolates impacts from other environmental or biological variables and focuses only on the temperature effect.

For each wetland type, we calculated the mean change in F_{CH_4} due to soil warming across all site years. We defined response ratio to warming by percentage change of F_{CH_4} under warmed and controlled conditions. Large differences between the LSTM and causal-LSTM existed in response to warming, especially for bogs (4.9% vs 21.8%) and fens (2.7% vs 10.1%) (Fig. 5). The differences in causal-LSTM predictions are significantly larger than those of LSTM for bog, fen, marsh and wet tundra sites ($p < 0.05$; Table S12). Overall, the LSTM model estimated lower methane emission in response to warming than causal-LSTM model, primarily due to the less important role of soil temperature in its internal model functions (Fig. 4a). Therefore, this work highlights the importance of considering causal relationships in modeling CH_4 emissions under a changing climate. We advocate the use of these types of causal relationship constraints for other ecosystem variables calculated through machine learning approaches (*e.g.*, FLUXNET-MTE GPP (Jung et al., 2011)). In addition, causality constrained ML models could serve as surrogate modules for efficient parameterization and high accuracy prediction, especially for processes that lack theoretical understanding and mathematical model structures.

5. Conclusions

Based on *in situ* eddy covariance measurements of daily CH_4 emissions (F_{CH_4}) at 30 eddy covariance sites in bog, fen, marsh, and wet tundra wetlands, we found consistent causal regulations from soil temperature on F_{CH_4} using a transfer entropy approach. We also confirmed important causal relationships with ecosystem respiration (RECO) and gross primary production at bog, fen, and marsh wetlands. The transfer entropy approach explicitly excludes confounding variables and therefore reduces the possibility that the observed causal relationship between F_{CH_4} and RECO or GPP was due to covariation with other environmental drivers, such as temperature (Chu et al., 2014; Knox et al., 2019). We then developed a predictive model that integrated the transfer entropy inferred causal relationships for F_{CH_4} simulations. The causality constrained model outperformed other baseline ML models in terms of accuracy (relative MAE and R); more importantly, we demonstrated that including underlying causal relationships in predicting F_{CH_4} under a 1°C soil warming could differ by up to a factor of 4, compared with traditional ML models. Our results highlighted that those causal relationships can be used to benchmark, evaluate, and improve wetland methane emission models. Our proposed causality constrained model could benefit large-scale upscaling, data gap-filling, and surrogate modeling of wetland CH_4 emissions within earth system land models.

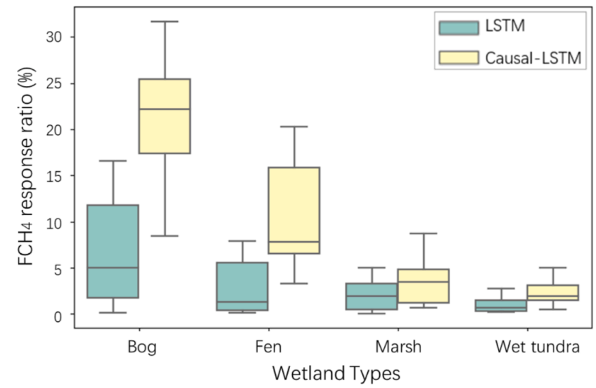

Fig. 5. F_{CH_4} response ratio to an imposed +1 °C soil warming of LSTM (green) and causal-LSTM (yellow) models. The boxes represent 25th to 75th percentiles, and the whiskers represent 5th to 95th percentiles of R or MAE for each wetland type.

Declaration of Competing Interest

The authors declare that they have no known competing financial interests or personal relationships that could have appeared to influence the work reported in this paper.

Data availability

Data will be made available on request.

Acknowledgments

This research was primarily supported by NASA Carbon Monitoring System grant (#NNH20ZDA001N) and the Reducing Uncertainties in Biogeochemical Interactions through Synthesis and Computation (RUBISCO) Scientific Focus Area Project, the latter is sponsored by the Earth and Environmental Systems Modeling (EESM) Program under the Office of Biological and Environmental Research of the US Department of Energy Office of Science. Min Chen acknowledges the support from NASA Terrestrial Ecology Arctic Boreal Vulnerability Experiment Phase 2 program (#80NSSC21K1702). Margaret Torn acknowledges the support from The Next-Generation Ecosystem Experiments (NGEE Arctic) project under the Office of Biological and Environmental Research in the DOE Office of Science. We acknowledge support from John Wesley Powell Center for Analysis and Synthesis of the U.S. Geological Survey ("Wetland FLUXNET Synthesis for Methane" working group). Any use of trade, firm, or product names is for descriptive purposes only and does not imply endorsement by the U.S. Government.

Supplementary materials

Supplementary material associated with this article can be found, in the online version, at doi:10.1016/j.agrformet.2022.109115.

References

Abdul Razak, F., Jensen, H.J., 2014. Quantifying 'causality'in complex systems: understanding transfer entropy. PLoS One 9 (6), e99462.
Alahi, A., et al., 2016. Social lstm: Human trajectory prediction in crowded spaces. In: Proceedings of the IEEE conference on computer vision and pattern recognition, pp. 961–971.
Bastviken, D., 2009. Methane.
Bergamaschi, P., et al., 2013. Atmospheric CH4 in the first decade of the 21st century: inverse modeling analysis using SCIAMACHY satellite retrievals and NOAA surface measurements. J. Geophys. Res. Atmos. 118 (13), 7350–7369.
Bergman, I., Klarqvist, M., Nilsson, M., 2000. Seasonal variation in rates of methane production from peat of various botanical origins: effects of temperature and substrate quality. FEMS Microbiol. Ecol. 33 (3), 181–189.

Bohrer, G. and Morin, T.H., 2020. FLUXNET-CH4 US-ORv Olentangy River Wetland Research Park, United States.
Boothroyd, I.M., Almond, S., Worrall, F., Davies, R., 2017. Assessing the fugitive emission of CH4 via migration along fault zones–comparing potential shale gas basins to non-shale basins in the UK. Sci. Total Environ. 580, 412–424.
Bouskill, N.J., Riley, W.J., Zhu, Q., Mekonnen, Z.A., Grant, R.F., 2020. Alaskan carbon-climate feedbacks will be weaker than inferred from short-term experiments. Nat. Commun. 11 (1), 1–12.
Bousquet, P., et al., 2006. Contribution of anthropogenic and natural sources to atmospheric methane variability. Nature 443 (7110), 439–443.
Brown, M.G., Humphreys, E.R., Moore, T.R., Roulet, N.T., Lafleur, P.M., 2014. Evidence for a nonmonotonic relationship between ecosystem-scale peatland methane emissions and water table depth. J. Geophys. Res. Biogeosci. 119 (5), 826–835.
Campbell, D., Goodrich, J., 2020. FLUXNET-CH4 NZ-Kop Kopuatai, New Zealand.
Castro-Morales, K., et al., 2018. Year-round simulated methane emissions from a permafrost ecosystem in Northeast Siberia. Biogeosciences 15 (9), 2691–2722.
Chadburn, S.E., et al., 2020. Modeled microbial dynamics explain the apparent temperature sensitivity of wetland methane emissions. Global Biogeochem. Cycles 34 (11), e2020GB006678.
Chang, K.-Y., Riley, W.J., Crill, P.M., Grant, R.F., Saleska, S.R., 2020. Hysteretic temperature sensitivity of wetland CH 4 fluxes explained by substrate availability and microbial activity. Biogeosciences 17 (22), 5849–5860.
Chang, K.-Y., et al., 2021. Substantial hysteresis in emergent temperature sensitivity of global wetland CH4 emissions. Nat. Commun. 12 (1), 1–10.
Chang, K.Y., et al., 2019. Methane production pathway regulated proximally by substrate availability and distally by temperature in a high-latitude mire complex. J. Geophys. Res. Biogeosci. 124 (10), 3057–3074.
Chen, H., Xu, X., Fang, C., Li, B., Nie, M., 2021. Differences in the temperature dependence of wetland CO_2 and CH_4 emissions vary with water table depth. Nat. Clim. Change 11 (9), 766–771.
Chen, J. and Chu, H., 2020. FLUXNET-CH4 US-WPT Winous Point North Marsh, United States.
Chen, Y.H., Prinn, R.G., 2006. Estimation of atmospheric methane emissions between 1996 and 2001 using a three-dimensional global chemical transport model. J. Geophys. Res. Atmos. 111 (D10).
Chu, H., et al., 2014. Net ecosystem methane and carbon dioxide exchanges in a Lake Erie coastal marsh and a nearby cropland. J. Geophys. Res. Biogeosci. 119 (5), 722–740.
Dean, J.F., et al., 2018. Methane feedbacks to the global climate system in a warmer world. Rev. Geophys. 56 (1), 207–250.
Delwiche, K.B., et al., 2021. FLUXNET-CH4: a global, multi-ecosystem dataset and analysis of methane seasonality from freshwater wetlands. Earth Syst. Sci. Data 13 (7), 3607–3689.
Desai, A.R. and Thom, J., 2020. FLUXNET-CH4 US-Los Lost Creek, United States.
Eichelmann, E. et al., 2020. FLUXNET-CH4 US-Tw4 Twitchell East End Wetland, United States.
Euskirchen, E., Bret-Harte, M. and Edgar, C., 2020. FLUXNET-CH4 US-ICs Imnavait Creek Watershed Wet Sedge Tundra, United States.
Euskirchen, E. and Edgar, C., 2020a. FLUXNET-CH4 US-BZB Bonanza Creek Thermokarst Bog, United States.
Euskirchen, E. and Edgar, C., 2020b. FLUXNET-CH4 US-BZF Bonanza Creek Rich Fen, United States.
Fan, L., et al., 2021. Active metabolic pathways of anaerobic methane oxidation in paddy soils. Soil Biol. Biochem. 156, 108215.
Gal, Y., Ghahramani, Z., 2016. A theoretically grounded application of dropout in recurrent neural networks. Adv. Neural Inf. Process. Syst. 29, 1019–1027.
Göckede, M., 2020. FLUXNET-CH4 RU-Ch2 Chersky reference, Russia.
Göckede, M., et al., 2019. Negative feedback processes following drainage slow down permafrost degradation. Global Change Biol. 25 (10), 3254–3266.
Goodrich, J., Campbell, D., Roulet, N., Clearwater, M., Schipper, L., 2015. Overriding control of methane flux temporal variability by water table dynamics in a Southern Hemisphere, raised bog. J. Geophys. Res. Biogeosci. 120 (5), 819–831.
Granberg, G., Mikkelä, C., Sundh, I., Svensson, B.H., Nilsson, M., 1997. Sources of spatial variation in methane emission from mires in northern Sweden: a mechanistic approach in statistical modeling. Global Biogeochem. Cycles 11 (2), 135–150.
Grant, R., Humphreys, E., Lafleur, P., 2015. Ecosystem CO_2 and CH_4 exchange in a mixed tundra and a fen within a hydrologically diverse Arctic landscape: 1. Modeling versus measurements. J. Geophys. Res. Biogeosci. 120 (7), 1366–1387.
Grant, R., Mekonnen, Z., Riley, W., Arora, B., Torn, M., 2017a. 2. Microtopography determines how CO2 and CH4 exchange responds to changes in temperature and precipitation at an Arctic polygonal tundra site: Mathematical modelling with Ecosys. J. Geophys. Res. Biogeosci. 122, 3174–3187.
Grant, R., et al., 2017b. I: Microtopography determines how active layer depths respond to changes in temperature and precipitation at an Arctic polygonal tundra site: Mathematical modelling with Ecosys. J. Geophys. Res. Biogeosci. 122, 3161–3173.
Guo, T., Lin, T., Antulov-Fantulin, N., 2019a. Exploring interpretable lstm neural networks over multi-variable data. In: International Conference on Machine Learning. PMLR, pp. 2494–2504.
Guo, T., Lin, T., Antulov-Fantulin, N., 2019b. Exploring interpretable lstm neural networks over multi-variable data. arXiv preprint arXiv:1905.12034.
Guyon, I., Weston, J., Barnhill, S., Vapnik, V., 2002. Gene selection for cancer classification using support vector machines. Mach. Learn. 46 (1), 389–422.
Hatala, J.A., Detto, M., Baldocchi, D.D., 2012a. Gross ecosystem photosynthesis causes a diurnal pattern in methane emission from rice. Geophys. Res. Lett. 39 (6), L06409.
Hatala, J.A., et al., 2012b. Greenhouse gas (CO2, CH4, H2O) fluxes from drained and flooded agricultural peatlands in the Sacramento-San Joaquin Delta. Agricul. Ecosyst. Environ. 150, 1–18.
Hemes, K.S., Chamberlain, S.D., Eichelmann, E., Knox, S.H., Baldocchi, D.D., 2018. A biogeochemical compromise: the high methane cost of sequestering carbon in restored wetlands. Geophys. Res. Lett. 45 (12), 6081–6091.
Hinkle, C.R. and Bracho, R., 2020. FLUXNET-CH4 US-DPW Disney Wilderness Preserve Wetland, United States.
Hochreiter, S., Schmidhuber, J., 1997. Long short-term memory. Neural Comput. 9 (8), 1735–1780.
Holm, G.O. et al., 2020. FLUXNET-CH4 US-LA2 Salvador WMA Freshwater Marsh, United States.
IPCC, 2013. Chapter 6: carbon and other biogeochemical cycles. Climate Change 2013 The Physical Science Basis. Cambridge University Press, Cambridge.
Irvin, J., et al., 2021. Gap-filling eddy covariance methane fluxes: comparison of machine learning model predictions and uncertainties at FLUXNET-CH4 wetlands. Agric. For. Meteorol. 308, 108528.
Iwata, H., Ueyama, M. and Harazono, Y., 2020. FLUXNET-CH4 US-Uaf University of Alaska, Fairbanks, United States.
Jackowicz-Korczyński, M., et al., 2010. Annual cycle of methane emission from a subarctic peatland. J. Geophys. Res. Biogeosci. 115 (G2).
Jansen, J., Friborg, T., Jammet, M. and Crill, P., 2020. FLUXNET-CH4 SE-St1 Stordalen grassland, Sweden.
Jauhiainen, J., Takahashi, H., Heikkinen, J.E., Martikainen, P.J., Vasander, H., 2005. Carbon fluxes from a tropical peat swamp forest floor. Global Change Biol. 11 (10), 1788–1797.
Jung, M., et al., 2011. Global patterns of land-atmosphere fluxes of carbon dioxide, latent heat, and sensible heat derived from eddy covariance, satellite, and meteorological observations. J. Geophys. Res. Biogeosci. 116 (G3).
Kantz, H., Schürmann, T., 1996. Enlarged scaling ranges for the KS-entropy and the information dimension. Chaos Interdiscip. J. Nonlinear Sci. 6 (2), 167–171.
Kim, Y., et al., 2020. Gap-filling approaches for eddy covariance methane fluxes: a comparison of three machine learning algorithms and a traditional method with principal component analysis. Global Change Biol. 26 (3), 1499–1518.
Kim, Y., et al., 2007. Assessment of winter fluxes of CO2 and CH4 in boreal forest soils of central Alaska estimated by the profile method and the chamber method: a diagnosis of methane emission and implications for the regional carbon budget. Tellus B: Chem. Phys. Meteorol. 59 (2), 223–233.
King, J.Y., Reeburgh, W.S., Regli, S.K., 1998. Methane emission and transport by arctic sedges in Alaska: results of a vegetation removal experiment. J. Geophys. Res. Atmos. 103 (D22), 29083–29092.
Knox, S.H., et al., 2021. Identifying dominant environmental predictors of freshwater wetland methane fluxes across diurnal to seasonal time scales. Global Change Biol. 27 (15), 3582–3604.
Knox, S.H., et al., 2019. FLUXNET-CH4 synthesis activity: objectives, observations, and future directions. Bull. Am. Meteorol. Soc. 100 (12), 2607–2632.
Knox, S.H., et al., 2016. Biophysical controls on interannual variability in ecosystem-scale CO_2 and CH_4 exchange in a California rice paddy. J. Geophys. Res. Biogeosci. 121 (3), 978–1001.
Koch, S., Jurasinski, G., Koebsch, F., Koch, M., Glatzel, S., 2014. Spatial variability of annual estimates of methane emissions in a Phragmites australis (Cav.) Trin. ex Steud. dominated restored coastal brackish fen. Wetlands 34 (3), 593–602.
Koebsch, F. and Jurasinski, G., 2020. FLUXNET-CH4 DE-Hte Huetelmoor, Germany.
Koffi, E.N., Bergamaschi, P., Alkama, R., Cescatti, A., 2020. An observation-constrained assessment of the climate sensitivity and future trajectories of wetland methane emissions. Sci. Adv. 6 (15).
Kullback, S., Leibler, R.A., 1951. On information and sufficiency. Annal. Math Stat. 22 (1), 79–86.
Li, F., et al., 2020. A hierarchical temporal attention-based LSTM encoder-decoder model for individual mobility prediction. Neurocomputing.
Li, F., Zhu, Q., Riley, W.J., Yuan, K., Wu, H., Gui, Z., 2022. Wetter California projected by CMIP6 models with observational constraints under a high GHG emission scenario. Earth's Future 10 (4) e2022EF002694.
Liang, Y., Ke, S., Zhang, J., Yi, X., Zheng, Y., 2018. Geoman: multi-level attention networks for geo-sensory time series prediction. IJCAI 3428–3434.
Liu, B.Y., et al., 2019. Using information theory to evaluate directional precipitation interactions over the West Sahel region in observations and models. J. Geophys. Res. Atmos. 124 (3), 1463–1473.
Lohila, A. et al., 2020. FLUXNET-CH4 FI-Lom Lompolojankka, Finland.
Matthes, J.H. et al., 2020. FLUXNET-CH4 US-Myb Mayberry Wetland, United States.
Mayer, H.P., Conrad, R., 1990. Factors influencing the population of methanogenic bacteria and the initiation of methane production upon flooding of paddy soil. FEMS Microbiol. Ecol. 6 (2), 103–111.
Melton, J.R., et al., 2013. Present state of global wetland extent and wetland methane modelling: conclusions from a model inter-comparison project (WETCHIMP). Biogeosciences 10 (2), 753–788.
Meyer, H., Reudenbach, C., Wöllauer, S., Nauss, T., 2019. Importance of spatial predictor variable selection in machine learning applications–moving from data reproduction to spatial prediction. Ecol. Modell. 411, 108815.
Mezbahuddin, M., Grant, R.F., Hirano, T., 2014. Modelling effects of seasonal variation in water table depth on net ecosystem CO_2exchange of a tropical peatland. Biogeosciences 11 (3), 577–599.
Mitra, B., et al., 2020. Spectral evidence for substrate availability rather than environmental control of methane emissions from a coastal forested wetland. Agric. For. Meteorol. 291, 108062.

Moraffah, R., Karami, M., Guo, R., Raglin, A., Liu, H., 2020. Causal interpretability for machine learning-problems, methods and evaluation. ACM SIGKDD Explorations Newsletter 22 (1), 18–33.

Morin, T., et al., 2014. Environmental drivers of methane fluxes from an urban temperate wetland park. J. Geophys. Res. Biogeosci. 119 (11), 2188–2208.

Morin, T.H., 2019. Advances in the eddy covariance approach to CH_4 monitoring over two and a half decades. J. Geophys. Res. Biogeosci. 124 (3), 453–460.

Nilsson, M.B. and Peichl, M., 2020. FLUXNET-CH4 SE-Deg Degero, Sweden.

Oertel, C., Matschullat, J., Zurba, K., Zimmermann, F., Erasmi, S., 2016. Greenhouse gas emissions from soils—a review. Geochemistry 76 (3), 327–352.

Pasut, C., Tang, F.H., Hamilton, D., Riley, W.J., Maggi, F., 2021. Spatiotemporal assessment of GHG emissions and nutrient sequestration linked to Agronutrient runoff in global wetlands. Global Biogeochem. Cycles 35 (4), e2020GB006816.

Pearl, J., 2019. The limitations of opaque learning machines. Possible Minds: Twenty-Five Ways of Looking at AI, pp. 13–19.

Peltola, O., et al., 2019. Monthly gridded data product of northern wetland methane emissions based on upscaling eddy covariance observations. Earth Sys. Sci. Data 11 (3), 1263–1289.

Prechelt, L., 1998. Early stopping-but when?, neural networks: tricks of the trade, lecture notes in computer science. Springer, Heidelberg, p. 1524.

Pries, C.E.H., Castanha, C., Porras, R., Torn, M., 2017. The whole-soil carbon flux in response to warming. Science 355 (6332), 1420–1423.

Qin, Y., et al., 2017. A dual-stage attention-based recurrent neural network for time series prediction. arXiv preprint arXiv:1704.02971.

Reichstein, M., et al., 2019. Deep learning and process understanding for data-driven Earth system science. Nature 566 (7743), 195–204.

Rey-Sanchez, A., Morin, T., Stefanik, K., Wrighton, K., Bohrer, G., 2018. Determining total emissions and environmental drivers of methane flux in a Lake Erie estuarine marsh. Ecol. Eng. 114, 7–15.

Riley, W., et al., 2011. Barriers to predicting changes in global terrestrial methane fluxes: analyses using CLM4Me, a methane biogeochemistry model integrated in CESM. Biogeosciences 8 (7), 1925–1953.

Rinne, J., et al., 2007. Annual cycle of methane emission from a boreal fen measured by the eddy covariance technique. Tellus B: Chem. Phys. Meteorol. 59 (3), 449–457.

Rinne, J., et al., 2018. Temporal variation of ecosystem scale methane emission from a boreal fen in relation to temperature, water table position, and carbon dioxide fluxes. Global Biogeochem. Cycles 32 (7), 1087–1106.

Rinne, J., et al., 2020. Effect of the 2018 European drought on methane and carbon dioxide exchange of northern mire ecosystems. Philos. Trans. R. Soc. B 375 (1810), 20190517.

Ruddell, B.L., Kumar, P., 2009. Ecohydrologic process networks: 1. Identification. Water Resour. Res. 45 (3).

Rumelhart, D.E., Hinton, G.E., Williams, R.J., 1986. Learning representations by back-propagating errors. Nature 323 (6088), 533–536.

Runge, J., et al., 2019a. Inferring causation from time series in Earth system sciences. Nat. Commun. 10 (1), 1–13.

Runge, J., Nowack, P., Kretschmer, M., Flaxman, S., Sejdinovic, D., 2019b. Detecting and quantifying causal associations in large nonlinear time series datasets. Sci. Adv. 5 (11), eaau4996.

Sachs, T. and Wille, C., 2020. FLUXNET-CH4 DE-Zrk Zarnekow, Germany.

Saunois, M., et al., 2020. The global methane budget 2000–2017. Earth Syst. Sci. Data 12 (3), 1561–1623.

Schaufler, G., et al., 2010. Greenhouse gas emissions from European soils under different land use: effects of soil moisture and temperature. Eur. J. Soil Sci. 61 (5), 683–696.

Schmid, H.P. and Klatt, J., 2020. FLUXNET-CH4 DE-SfN Schechenfilz Nord, Germany.

Schreiber, T., 2000. Measuring information transfer. Phys. Rev. Lett. 85 (2), 461.

Schuur, E.A., et al., 2008. Vulnerability of permafrost carbon to climate change: implications for the global carbon cycle. Bioscience 58 (8), 701–714.

Shortt, R., Hemes, K., Szutu, D., Verfaillie, J. and Baldocchi, D., 2020. FLUXNET-CH4 US-SNE Sherman Island Restored Wetland, United States.

Song, C., Sun, L., Huang, Y., Wang, Y., Wan, Z., 2011. Carbon exchange in a freshwater marsh in the Sanjiang Plain, northeastern China. Agric. For. Meteorol. 151 (8), 1131–1138.

Sonnentag, O. and Helbig, M., 2020a. FLUXNET-CH4 CA-SCB Scotty Creek Bog, Canada.

Sonnentag, O. and Helbig, M., 2020b. FLUXNET-CH4 CA-SCC Scotty Creek Landscape, Canada.

Spirtes, P., Glymour, C.N., Scheines, R., Heckerman, D., 2000. Causation, prediction, and search. MIT press.

Strachan, I.B., Nugent, K.A., Crombie, S., Bonneville, M.C., 2015. Carbon dioxide and methane exchange at a cool-temperate freshwater marsh. Environ. Res. Lett. 10 (6), 065006.

Ström, L., Tagesson, T., Mastepanov, M., Christensen, T.R., 2012. Presence of Eriophorum scheuchzeri enhances substrate availability and methane emission in an Arctic wetland. Soil Biol. Biochem. 45, 61–70.

Sturtevant, C., et al., 2016. Identifying scale-emergent, nonlinear, asynchronous processes of wetland methane exchange. J. Geophys. Res. Biogeosci. 121 (1), 188–204.

Tao, J., Zhu, Q., Riley, W.J., Neumann, R.B., 2020. Improved ELMv1-ECA simulations of zero-curtain periods and cold-season CH_4 and CO_2 emissions at Alaskan Arctic Tundra Sites. Cryosphere Discuss. 1–48.

Torn, M. and Dengel, S., 2020. FLUXNET-CH4 US-NGB NGEE Arctic Barrow, United States.

Turetsky, M.R., et al., 2014. A synthesis of methane emissions from 71 northern, temperate, and subtropical wetlands. Global Change Biol. 20 (7), 2183–2197.

Turner, J., Desai, A.R., Thom, J., Wickland, K., 2021. Lagged wetland CH_4 flux response in a historically wet year. J. Geophys. Res.: Biogeosci. 126 (11), e2021JG006458.

Ueyama, M., Hirano, T. and Kominami, Y., 2020. FLUXNET-CH4 JP-BBY Bibai bog, Japan.

Valach, A.C. et al., 2020. FLUXNET-CH4 US-Tw1 Twitchell Wetland West Pond, United States.

Vaswani, A., et al., 2017. Attention is all you need. Adv. Neural Inf. Process. Syst. 5998–6008.

Vesala, T., Tuittila, E.-S., Mammarella, I. and Alekseychik, P., 2020a. FLUXNET-CH4 FI-Si2 Siikaneva-2 Bog, Finland.

Vesala, T., Tuittila, E.-S., Mammarella, I. and Rinne, J., 2020b. FLUXNET-CH4 FI-Sii Siikaneva, Finland.

Villa, J.A., et al., 2020. Plant-mediated methane transport in emergent and floating-leaved species of a temperate freshwater mineral-soil wetland. Limnol. Oceanogr. 65 (7), 1635–1650.

Villa, J.A., et al., 2021. Ebullition dominates methane fluxes from the water surface across different ecohydrological patches in a temperate freshwater marsh at the end of the growing season. Sci. Total Environ. 767, 144498.

Wahlen, M., 1993. The global methane cycle. Annu. Rev. Earth Planet. Sci. 21 (1), 407–426.

Wania, R., et al., 2013. Present state of global wetland extent and wetland methane modelling: methodology of a model inter-comparison project (WETCHIMP). Geoscientific Model Dev. 6 (3), 617–641.

Whalen, S., 2005. Biogeochemistry of methane exchange between natural wetlands and the atmosphere. Environ. Eng. Sci. 22 (1), 73–94.

Whiting, G.J., Chanton, J.P., 1993. Primary production control of methane emission from wetlands. Nature 364 (6440), 794–795.

Xu, X., et al., 2016. Reviews and syntheses: four decades of modeling methane cycling in terrestrial ecosystems. Biogeosciences 13 (12), 3735–3755.

Yuan, K., et al., 2021. Deforestation reshapes land-surface energy-flux partitioning. Environ. Res. Lett. 16 (2), 024014.

Yuan, K., Zhu, Q., Riley, W.J., Li, F., Wu, H., 2022. Understanding and reducing the uncertainties of land surface energy flux partitioning within CMIP6 land models. Agric. For. Meteorol. 319, 108920.

Yvon-Durocher, G., et al., 2014. Methane fluxes show consistent temperature dependence across microbial to ecosystem scales. Nature 507 (7493), 488–491.

Zhang, Z., et al., 2017. Emerging role of wetland methane emissions in driving 21st century climate change. Proc. Natl. Acad. Sci. 114 (36), 9647–9652.

Zona, D., et al., 2016. Cold season emissions dominate the Arctic tundra methane budget. Proc. Natl. Acad. Sci. 113 (1), 40–45.

Zona, D. and Oechel, W.C., 2020a. FLUXNET-CH4 US-Beo Barrow Environmental Observatory (BEO) tower, United States.

Zona, D. and Oechel, W.C., 2020b. FLUXNET-CH4 US-Bes Barrow-Bes (Biocomplexity Experiment South tower), United States.

Zona, D. and Oechel, W.C., 2020c. FLUXNET-CH4 US-Ivo Ivotuk, United States.